*Human Molecular Genetics, 2014, Vol. 23, No. 22* **5950–5960**
*doi:10.1093/hmg/ddu319*
*Advance Access published on June 30, 2014*

# Altered spatio-temporal dynamics of RNase H2 complex assembly at replication and repair sites in Aicardi–Goutières syndrome

**Barbara Kind[1,†], Britta Muster[3,†], Wolfgang Staroske[2], Henry D. Herce[4], René Sachse[5], Alexander Rapp[3], Franziska Schmidt[1], Sarah Koss[1], M. Cristina Cardoso[3,*] and Min Ae Lee-Kirsch[1,*]**

[1]Department of Pediatrics, Medizinische Fakultät Carl Gustav Carus and [2]Biotechnology Center, Technische Universität Dresden, 01307 Dresden, Germany, [3]Department of Biology, Technische Universität Darmstadt, 64287 Darmstadt, Germany, [4]Department of Physics, Applied Physics and Astronomy, Rensselaer Polytechnic Institute, New York 12180-3590, USA and [5]Institute of Earth and Environmental Science, Potsdam University, 14476 Potsdam, Germany

Received May 6, 2014; Revised and Accepted June 17, 2014

**Ribonuclease H2 plays an essential role for genome stability as it removes ribonucleotides misincorporated into genomic DNA by replicative polymerases and resolves RNA/DNA hybrids. Biallelic mutations in the genes encoding the three RNase H2 subunits cause Aicardi–Goutières syndrome (AGS), an early-onset inflammatory encephalopathy that phenotypically overlaps with the autoimmune disorder systemic lupus erythematosus. Here we studied the intracellular dynamics of RNase H2 in living cells during DNA replication and in response to DNA damage using confocal time-lapse imaging and fluorescence cross-correlation spectroscopy. We demonstrate that the RNase H2 complex is assembled in the cytosol and imported into the nucleus in an RNase H2B-dependent manner. RNase H2 is not only recruited to DNA replication foci, but also to sites of PCNA-dependent DNA repair. By fluorescence recovery after photobleaching, we demonstrate a high mobility and fast exchange of RNase H2 at sites of DNA repair and replication. We provide evidence that recruitment of RNase H2 is not only PCNA-dependent, mediated by an interaction of the B subunit with PCNA, but also PCNA-independent mediated via the catalytic domain of the A subunit. We found that AGS-associated mutations alter complex formation, recruitment efficiency and exchange kinetics at sites of DNA replication and repair suggesting that impaired ribonucleotide removal contributes to AGS pathogenesis.**

## INTRODUCTION

Ribonuclease H2 (RNase H2) belongs to the RNase H family of endoribonucleases which cleave the RNA moiety in RNA/DNA hybrids. Unlike RNase H1, RNase H2 can also hydrolyze the 5′-phosphodiester bond of a single ribonucleotide embedded in a DNA duplex (1). Previous studies in yeast and mice have shown that RNase H2 plays an essential role in the maintenance of genome integrity (2–4). It facilitates the removal of ribonucleotides misincorporated into genomic DNA by replicative polymerases by a ribonucleotide excision repair (RER) mechanism (5–7). Indeed, ribonucleotides were shown to represent the most frequent DNA base lesion (one per 7000 base pairs) in replicating mammalian cells (3). If left unrepaired, misincorporated ribonucleotides render the DNA backbone susceptible to strand cleavage leading to genome instability (3,8–11). In mice with complete RNase H2 deficiency, accumulation of ribonucleotides in genomic DNA causes embryonic lethality due to a p53-dependent DNA damage response (3,4). In addition, RNase H2 has also been implicated in the resolution of R-loops, deleterious RNA:DNA hybrid structures that can form during transcription (6,12–14).

The human RNase H2 forms a heterotrimeric complex consisting of the catalytic RNase H2A subunit, which is characterized by a metal binding DEDD motif (D24, E35, D141, D169), and two auxiliary subunits RNase H2B and RNase H2C (1,15–17).

*To whom correspondence should be addressed. Tel: +49 351 458 6887; Fax: +49 351 458 6333; Email: minae.lee-kirsch@uniklinikum-dresden.de (M.L.-K.); Tel: +49 6151 16 2377; Fax: +49 6151 16 2375; Email: cardoso@bio.tu-darmstadt.de (M.C.C.)
†B.K. and B.M. contributed equally to this work.

Analysis of the crystal structure of RNase H2 complex demonstrated that the three subunits are arranged in one line with the C subunit located in the center (Fig. 1A). The auxiliary B and C subunits adopt an interwoven triple β-barrel folded together with the C-terminal extension of the A subunit located on the C-terminal half of RNase H2C (15,17,18). In eukaryotic cells, all three subunits are required for enzymatic activity (19). Although the exact functions of the B and C subunits are not fully understood, it is likely that both subunits are involved in interactions with other proteins. The B subunit was shown to possess a PIP-box motif at its C-terminus, which mediates interaction with the DNA polymerase processivity factor proliferating cell nuclear antigen (PCNA) consistent with a role for RNase H2 in DNA replication and repair (20,21). Biallelic mutations in the genes encoding the three RNase H2 subunits (*RNASEH2A*, *RNASEH2B*, *RNASEH2C*) cause Aicardi–Goutières syndrome (AGS2, AGS3, AGS4; OMIM 610181, 610329, 610333), an autosomal recessive inflammatory encephalopathy characterized by basal ganglia calcification, myelin defects and brain atrophy (22). The phenotype of AGS mimics *in utero* acquired viral infection and overlaps with the autoimmune disorder systemic lupus erythematosus (SLE). Features common to both disorders include activation of the antiviral cytokine interferon (IFN)-α, cutaneous chilblain lesions, arthritis, antinuclear antibodies, reduced complement and hematological abnormalities (23).

AGS is also caused by biallelic mutations in the 3′ repair exonuclease 1 (*TREX1*) (24), the dNTP-degrading triphosphohydrolase *SAMHD1* (25), the RNA-editing enzyme *ADAR1* (26) and *IFIHI* (27). Furthermore, heterozygous mutations in *TREX1* and *SAMHD1* cause familial chilblain lupus or SLE (28–31). It is thought that defects in RNase H2, TREX1, SAMHD1, ADAR1 and IFIHI result in the intracellular accrual of nucleic acid species or an enhanced sensing of nucleic acids which triggers a type I-IFN-dependent innate immune response leading to inflammation and autoimmunity (32,33). The association of RNase H2 with autoimmunity points to an important role of the nucleic acid metabolism in the prevention of inadequate immune responses and implicate defects in DNA replication and repair in the pathogenesis of autoimmunity. In this study, we analyzed the assembly and recruitment of the RNase H2 complex to sites of DNA replication and repair in order to gain more insight into the spatio-temporal dynamics of RNase H2 in living cells.

## RESULTS AND DISCUSSION

### Intracellular distribution and assembly of the RNase H2 complex

In contrast to prokaryotic RNase HII, which acts as a monomeric enzyme, eukaryotic RNase H2 functions as a complex composed of three distinct subunits, all of which are required for full catalytic activity (19,20). In agreement with previous reports showing that RNase H2 is a nuclear protein, all three wild-type RNase H2 subunits N-terminally labeled with different fluorophores were localized in the nucleus (Fig. 1B). In the absence of either the A or C subunit, respectively, the B subunit remained nuclear, while the corresponding third subunit was also found in the cytosol. In contrast, both the A and C subunits were diffusely distributed throughout the entire cell when expressed in the absence of the B subunit indicating that the B subunit is required for nuclear targeting of the RNase H2 complex. Expression of the *RNASEH2C* mutant D115fs (C_D115fs) which is translated into a C-terminally truncated protein along with the wild-type A and B subunits also led to a diffuse distribution of the A and the mutant C subunit suggesting that formation of stable complexes requires an intact C subunit. Co-expression of the mutants A_G37S, B_ΔPIP, B_A177T, C_R69W and C_D39Y with the corresponding wild-type subunits did not alter the subcellular distribution of the RNase H2 complex demonstrating that these mutations do not impair formation and nuclear targeting of the heterotrimers (data not shown).

For further quantification, we determined the absolute number of fluorescent particles of the wild-type RNase H2 complex within a confocal volume both in the cytoplasm and the nucleus by fluorescence correlation spectroscopy (Fig. 1C). In the absence of the B subunit (WTΔB), the nuclear/cytoplasmatic ratio of RNase H2A and RNase H2C strongly decreased from $11.4 \pm 8.1$ to $1.9 \pm 0.8$ and from $15.4 \pm 12.5$ to $1.8 \pm 0.8$, respectively, suggesting passive diffusion of these subunits across the nuclear membrane. A lack of either the A (WTΔA) or the C (WTΔC) subunit also led to a significant decrease of the nuclear/cytoplasmatic ratio of the corresponding other subunits, although the B subunit remained mainly nuclear in both conditions. In the presence of the deletion mutant C_D115fs, the nuclear/cytoplasmatic ratio of both the A and the truncated C subunit decreased nearly to the level of free diffusion, which is consistent with the loss of heterotrimer formation. These findings suggest that the RNase H2 heterotrimer assembles within the cytosol and that the import and/or retention of the RNase H2 complex into the nucleus is mediated by the B subunit.

### RNase H2 complex stability in living cells

Except for the G37S mutation in the A subunit, which is catalytically inactive when tested on a single ribonucleotide-containing oligonucleotide, all other AGS-associated mutations studied so far were shown to be capable of hydrolyzing a DNA/DNA duplex containing one ribonucleotide *in vitro* (15,17,18,20,34,35) indicating that additional parameters underlie the impairment of RNase H2 function in AGS. Indeed, previous studies have demonstrated an effect of AGS-associated RNase H2 mutations on complex stability based on thermal stability assays using recombinant proteins (15,18). We therefore analyzed complex stability by assessing the interaction of individual RNase H2 subunits using fluorescence cross-correlation spectroscopy (FCCS) at the single-molecule level in living cells. Measureable cross-correlation within the nucleus of cells co-expressing either monomeric EGFP and mCherry (negative control) or a mCherry-EGFP tandem construct (positive control) ranged from $0.3 \pm 1.3\%$ for monomeric EGFP and mCherry to an average maximum of $36.6 \pm 2.5\%$ for the mCherry-EGFP tandem construct (Fig. 1D). We next co-transfected all three fluorescently tagged RNase H2 subunits and determined cross-correlation between each EGFP- and mCherry-tagged subunit combination (AB, AC, BC). The corresponding third subunit was ECFP-labeled for visual control. We observed high cross-correlation values in the range of the mCherry-EGFP tandem construct between $34.5 \pm 7.9\%$ for AB, $36.3 \pm 7.9\%$ for AC and $37.8 \pm 5.9\%$ for BC, respectively,

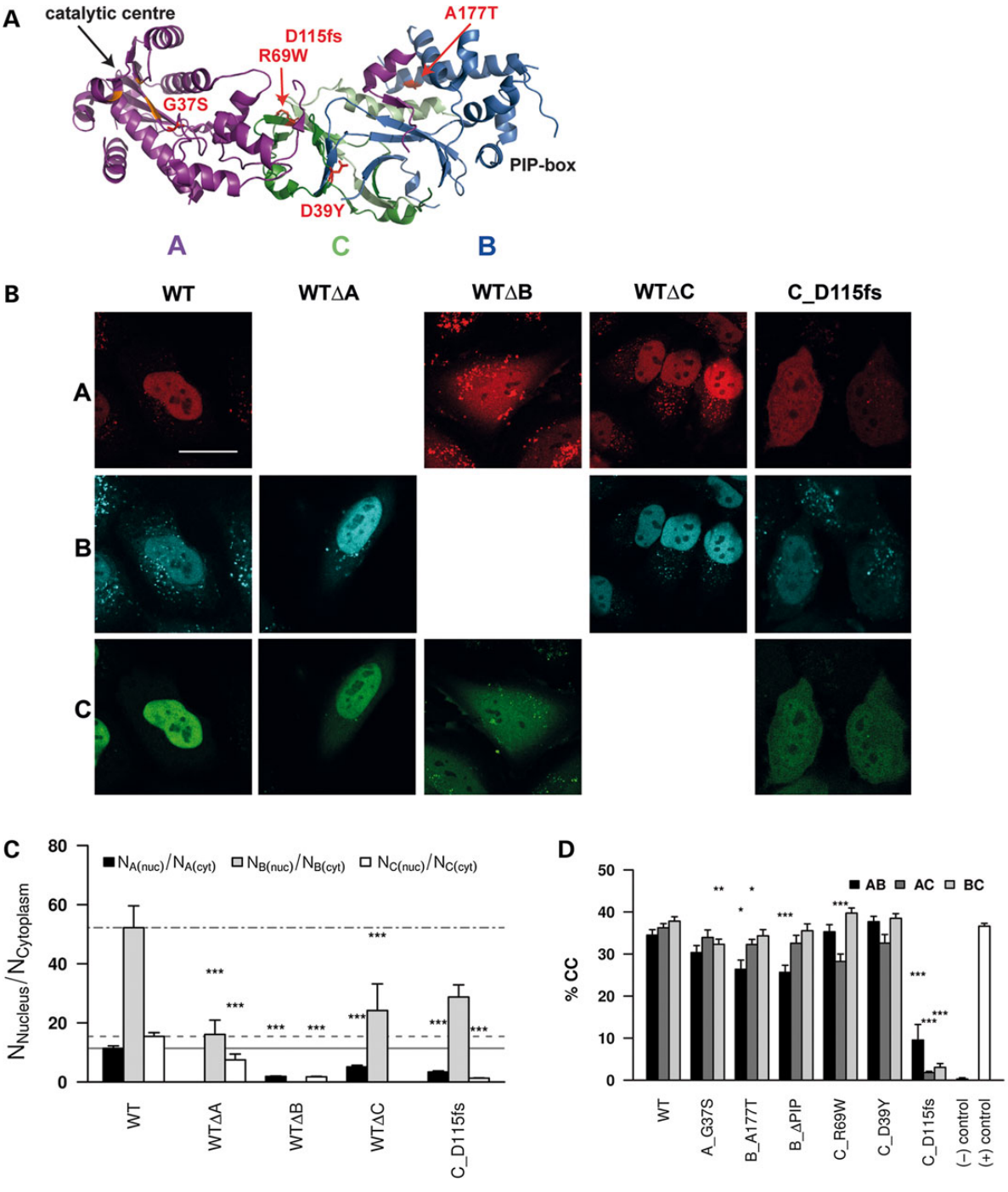


**Figure 1.** Subcellular localization and complex stability of the RNase H2 complex. (**A**) Position of AGS-associated mutations analyzed in this study within the human RNase H2 structure (PBD 3P56). G37S is located in the active center of the catalytic subunit A (purple). The common A177T is located in subunit B (blue) containing a PIP-box motif. D39Y, R69W and D115fs are positioned in the RNase H2C subunit (green). (**B**) Nuclear localization of the RNase H2 heterotrimer is dependent on the B subunit. Fluorescently tagged RNase H2 subunits target to the nucleus in HeLa cells. In the absence of the B subunit, the other subunits are diffusely distributed throughout the cell. Co-expression of fluorescently tagged C_D115fs along with the corresponding wild-type subunits leads to a diffuse distribution of all three subunits both within the nucleus and cytosol indicating impaired complex formation. The fluorescence of individual subunits was color-coded as follows: A (red), B (blue), C (green). Scale bar: 20 μm. (**C**) Nuclear/cytoplasmatic ratio of EGFP- and mCherry-tagged RNase H2 subunits measured by FCS. N: number of molecules. Wilcoxon–Mann–Whitney test, $^{*}P < 0.05$, $^{**}P < 0.01$, $^{***}P < 0.001$. Shown are the means ± standard error of the mean of at least 10 cells measured in at least two independent experiments. (**D**) RNase H2 complex stability analyzed by FCCS for each EGFP- and mCherry-labeled subunit combination (AB, AC, BC). Shown are the in cross-correlation (%CC) for each subunit combination compared with the wild-type RNase H2 complex. Mutations A_G37S, B_A177T, B_ΔPIP and C_R69W exhibited a reduction of cross-correlation for at least one subunit combination. Mutant C_D115fs shows a strongly decreased cross-correlation for each subunit combination. Wilcoxon–Mann–Whitney test, $^{*}P < 0.05$, $^{**}P < 0.01$, $^{***}P < 0.001$. Shown are the means ± standard error of the mean of at least 10 cells measured in at least two independent experiments.

indicating that all subunits were interacting with each other forming the heterotrimeric complex. Thus, within the nucleus, RNase H2 is exclusively found as a fully assembled complex. We next examined the effect of the AGS-associated mutations as well as the artificial B_ΔPIP mutant on cross-correlation between individual subunits. As shown in Figure 1D, the mutants A_G37S, B_A177T, C_R69W and B_ΔPIP significantly reduced the cross-correlation for at least one out of three subunit combinations indicating an effect on complex stability despite the preserved ability of these mutants to form a heterotrimer. While C_D39Y had no measurable effect on complex stability in living cells, the truncated subunit C_D115fs showed a complete loss of interaction for all three RNase H2 subunit combinations consistent with a lack of complex formation (Fig. 1D).

### Recruitment of RNase H2 to sites of DNA damage

To investigate the recruitment of RNase H2 to sites of DNA damage, we co-transfected HeLa cells stably expressing mCherry-tagged PCNA with each of the three EGFP-tagged RNase H2 subunits along with the respective un-tagged subunits and microirradiated the cells with a 405 nm laser to inflict localized DNA damage (36). The ring-shaped homotrimeric PCNA encircles and slides along DNA at replication forks acting as a 'sliding clamp' that guides coordinated assembly of factors involved in DNA replication and repair (36). Within 4 s post-irradiation, PCNA accumulated at sites of DNA damage indicating activation of PCNA-dependent DNA repair pathways. This was accompanied by fast recruitment of the RNase H2 complex to sites of DNA damage within the same time frame, as shown by confocal time-lapse microscopy (Fig. 2A and B). Quantification of accumulation revealed a similar kinetic behavior of all three wild-type subunits (Fig. 2B). Although RNase H2 complexes containing the catalytically inactive A_G37S mutant accumulated at DNA repair foci, the kinetic behavior showed a significantly reduced plateau compared with wild-type RNase H2 suggesting inefficient recruitment or retention at DNA repair sites. Accumulation of complexes containing the mutants B_A177T, C_D39Y or C_R69W was similar to that of the wild-type complex (Fig. 2C and D). Recruitment of RNase H2 to DNA replication foci has been shown to be mediated by an interaction of the PIP-box motif in the B subunit with PCNA (20,21). Consistent with this, the B_ΔPIP mutant showed no appreciable accumulation at DNA damage sites (Fig. 2D and F). Likewise, the C_D115fs did not accumulate at repair foci suggesting that complex integrity is important for binding to sites of DNA repair (Fig. 2E and F).

To gain further insight into the dynamics of RNase H2 recruited to repair sites, we studied the binding behavior of RNase H2 at sites of irradiation-induced DNA damage by fluorescence recovery after photobleaching (FRAP). During the FRAP experiments, the fluorescent tags of the fusion proteins were irreversibly bleached in a defined nuclear area and the exchange of bleached proteins with the surrounding unbleached ones was measured by monitoring the signal recovery. To this end, we allowed the proteins to accumulate for 200 s following microirradiation with a 405 nm laser prior to photobleaching with 488 and 561 nm. At this time point, the maximal accumulation had been reached (Fig. 3) and hence the signal recovery reflected the steady-state exchange rate. Fluorescence recovery was then measured every 200 ms (Fig. 3A). To assess the mobility of non-accumulated nucleoplasmic RNase H2 complexes, control FRAP experiments were performed in non-irradiated nuclei of non-S phase cells using the same conditions (Fig. 3B and C). Consistent with a tight binding to DNA, PCNA exhibited a very slow recovery at sites of DNA damage (37). In contrast, RNase H2 showed full recovery within 3 s after bleaching (Fig. 3A–C). To quantify protein exchange, half-times of full recovery for all mutant subunits were calculated. Indeed, exchange rates for all RNase H2 subunits at repair sites did not differ from those in non-irradiated areas (Fig. 3C) indicating a very short retention and an immediate release of the enzyme at repair sites. This dynamic behavior is consistent with previous studies showing that PCNA remains stably bound over a long time period at DNA damage sites, whereas PCNA interacting proteins such as DNA ligase I show a high turnover (38). These findings also demonstrate a role of RNase H2 in pathways of PCNA-dependent DNA repair and suggest that it might be involved in the removal of ribonucleotides misincorporated during gap-filling DNA synthesis.

### Association of RNase H2 with the DNA replication machinery

The far vast majority of DNA synthesis occurs during DNA replication in S phase. During this process, ribonucleotides were shown to be incorporated by the DNA polymerases δ and ε at an estimated rate of one ribonucleotide per 7000 bases and to be subsequently repaired by the RNase H2-dependent RER pathway (6,7,13). In addition, RNase H2 is capable of resolving R-loops, harmful RNA/DNA hybrid structures which can form during transcription (6,12–14). To further explore the dynamics of RNase H2 recruitment to replication sites, we analyzed the mobility and binding characteristics of individual EGFP-tagged RNase H2 subunits co-expressed with the corresponding other subunits in replicating HeLa cells stably expressing mCherry-PCNA. Consistent with previous reports, all wild-type subunits accumulated at replication foci as shown by colocalization with PCNA (Fig. 4A). The B_ΔPIP mutant showed no appreciable colocalization with PCNA in S phase confirming a role of the PIP-Box motif for PCNA binding. In agreement with a lack of complex formation, no accumulation of the C_D115fs mutant at replication foci was observed. All other mutants colocalized with PCNA indicating recruitment to replication sites (Fig. 4A). Interestingly, although the catalytically impaired mutant A_G37S accumulated at replication sites, colocalization with PCNA appeared somewhat blurred compared with wild-type RNase H2 (Fig. 4A). To analyze the colocalization between the RNase H2 subunits and PCNA in a quantitative manner, we used the colocalization coefficient $H_{coeff}$, which quantifies the spatial correlation between two fluorescent molecules as a function of the distance between the molecules (39). If two proteins within this distance are attracted to each other or are positively correlated $H_{coeff}$ is larger than 1. If they do not interact and are randomly distributed, the $H_{coeff}$ is 1, while values of $H_{coeff} < 1$ indicate repulsion between molecules (39). Determination of the $H_{coeff}$ revealed significantly reduced values for the mutants A_G37S, B_ΔPIP and C_D115fs compared with the corresponding wild-type subunits

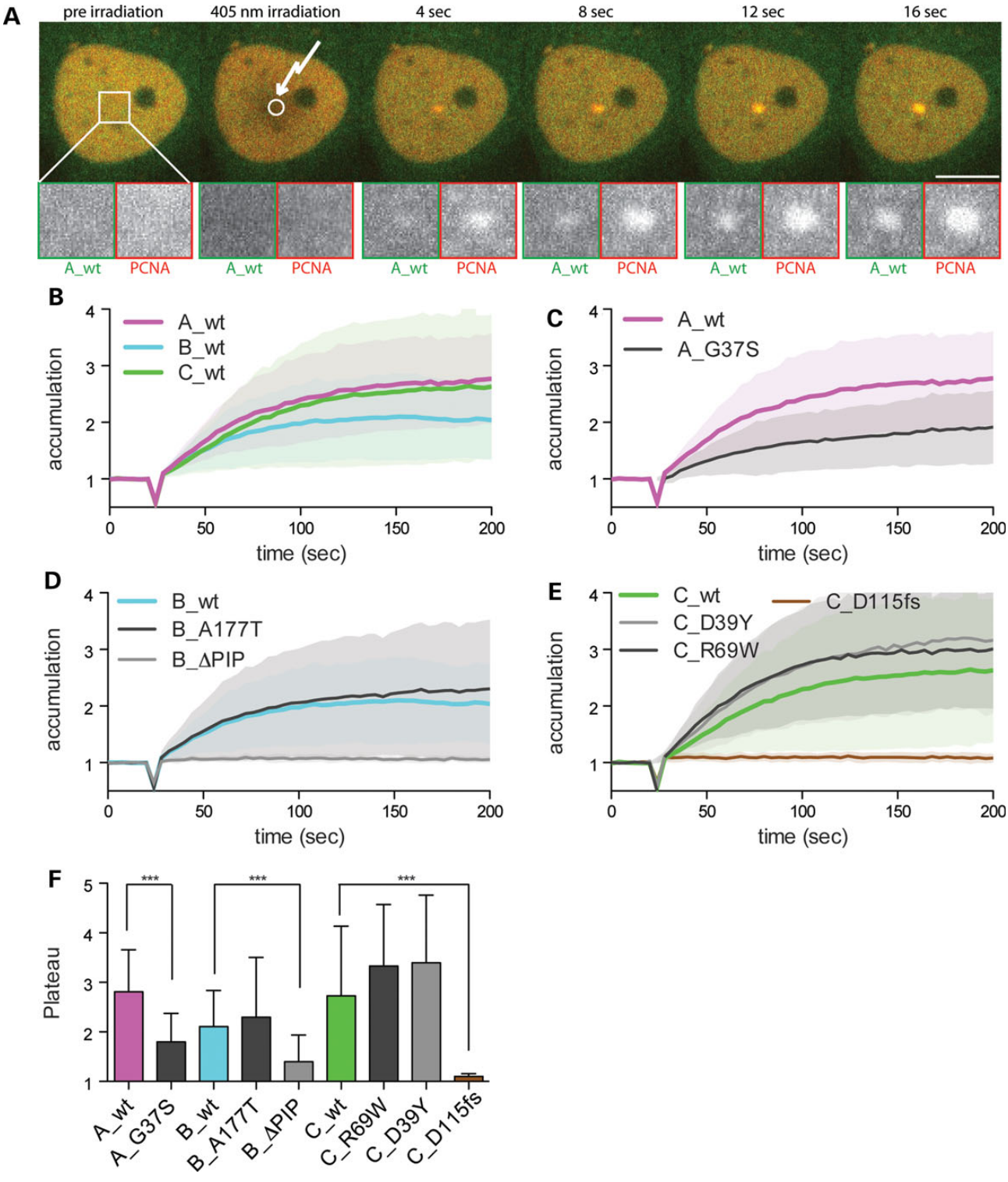


**Figure 2.** Recruitment of RNase H2 to sites of DNA damage. (**A**) Live-cell imaging of microirradiated HeLa cells expressing mCherry-PCNA and EGFP-RNase H2A along with the untagged B and C subunits. Pictures were taken every 4 s. RNase H2 accumulates at sites of DNA damage shown by colocalization with PCNA. Scale bar: 10 μm. (**B**–**E**) Accumulation kinetics of the wild-type and mutated RNase H2 complexes to sites of DNA damage. (**F**) Plateau level of accumulation curves. Wilcoxon–Mann–Whitney test, $^{*}P < 0.05$, $^{**}P < 0.01$, $^{***}P < 0.001$. Shown are the means ± standard deviation of at least five cells measured in at least two independent experiments. Color-shaded areas and error bars represent standard deviation.

(Fig. 4B). While the $H_{coeff}$ for C_D115fs was close to 1 suggesting random distribution, the $H_{coeff}$ for A_G37S was only slightly reduced compared with the wild-type A subunit consistent with the observed diminished focality. Remarkably, the B_ΔPIP mutant showed a significantly higher $H_{coeff}$ than the C_D115fs mutant ($P = 0.0006$) indicating some residual

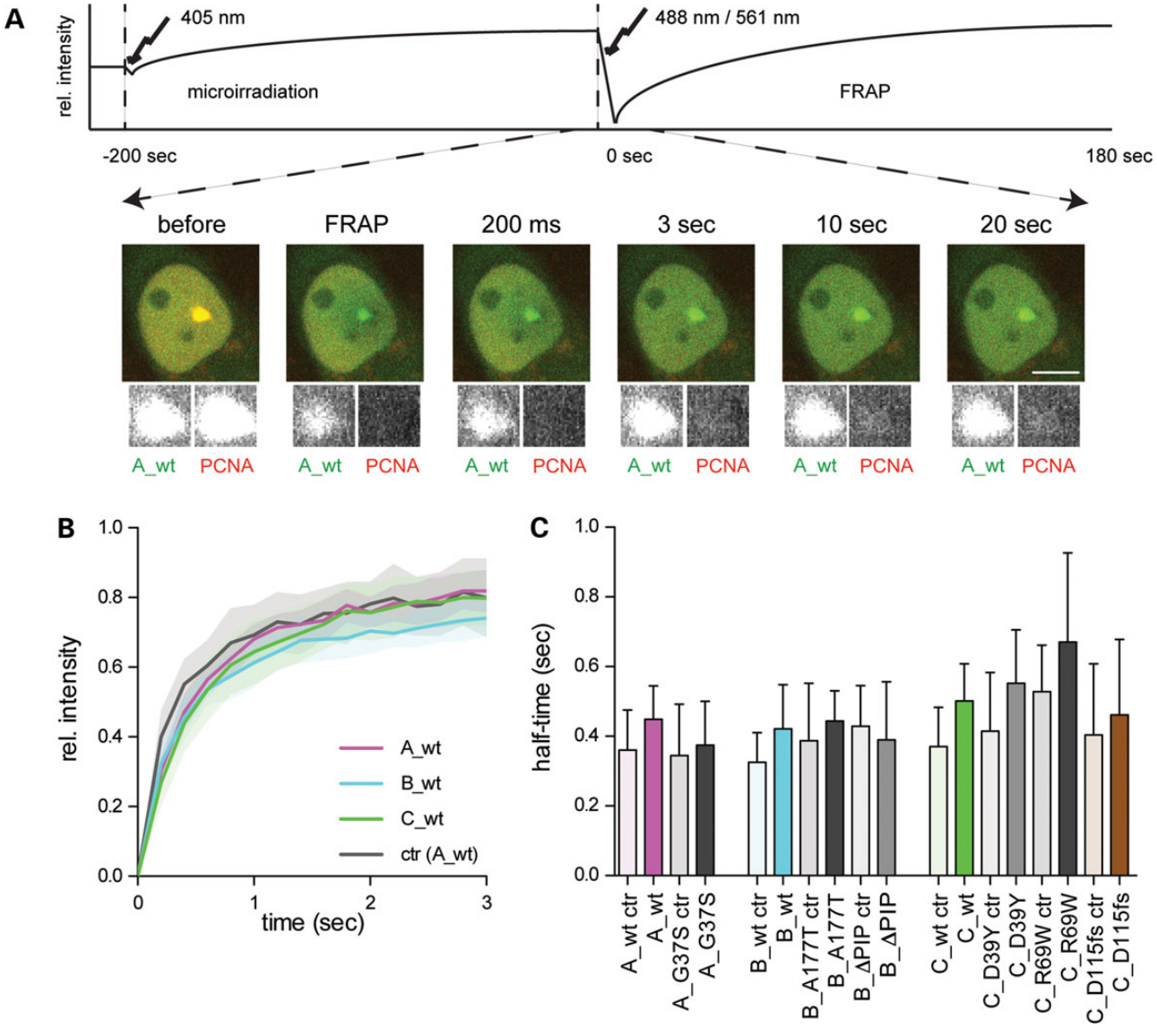


**Figure 3.** Dynamics of RNase H2 at repair sites. (**A**) Scheme of experimental setup of FRAP after microirradation of HeLa cells expressing mCherry-PCNA (PCNA) and EGFP-RNase H2A (A_wt) along with the untagged B and C subunits. Scale bar: 10 μm. (**B**) FRAP recovery of each RNase H2 subunit (A_wt, B_wt, C_wt) at microirradiated sites. Control FRAP measurements were performed in non-irradiated nucleoplasm. Shown is the FRAP recovery for the wild-type A subunit (ctr (A_wt)). Color-shaded areas represent standard deviation. (**C**) Half times determined from FRAP recovery curves. Wilcoxon–Mann–Whitney test, $^{*}P < 0.05$, $^{**}P < 0.01$, $^{***}P < 0.001$. Indicated are the means ± standard deviation of at least five cells measured in at least two independent experiments.

binding of this mutant at replication sites despite loss of the PIP-box motif.

We next examined the dynamics of RNase H2 recruitment to DNA during replication using FRAP at replication foci in S phase cells. FRAP control experiments were performed in nuclei of non-S phase cells to monitor the mobility of RNase H2 complexes in the absence of DNA replication. As expected, PCNA exhibited a very slow turnover at replication sites (40). Like at sites of DNA repair, RNase H2A signal at replication foci was fully recovered within 3 s (Fig. 5A). However, RNase H2 complexes exhibited a slower recovery at replication sites as shown by a reduced mobility compared with the corresponding non-S phase controls with a half-time of 0.72 ± 0.29s at replication sites versus 0.35 ± 0.1s in non-S phase cells ($P = 0.0001$) (Fig. 5B–E). This increase in retention may reflect the much higher presence of ribonucleotides in genomic DNA after DNA replication compared with gap-filling DNA synthesis during repair. Compared with the wild-type C subunit, the C_D115fs mutant exhibited a faster turnover at sites of DNA replication and showed the same mobility in replicating and non-replicating cells (Fig. 5D and E). All other mutant complexes displayed a significant delay in turnover at replication sites compared with non-replicating cells (Fig. 5B, C and E). Notably, also the catalytically inactive A_G37S mutant exhibited a faster turnover at sites of DNA replication compared with the wild-type (Fig. 5B and E). Thus, the reduced accumulation and retention of the A_G37S mutant suggest that a direct interaction of the catalytic domain with DNA is important for

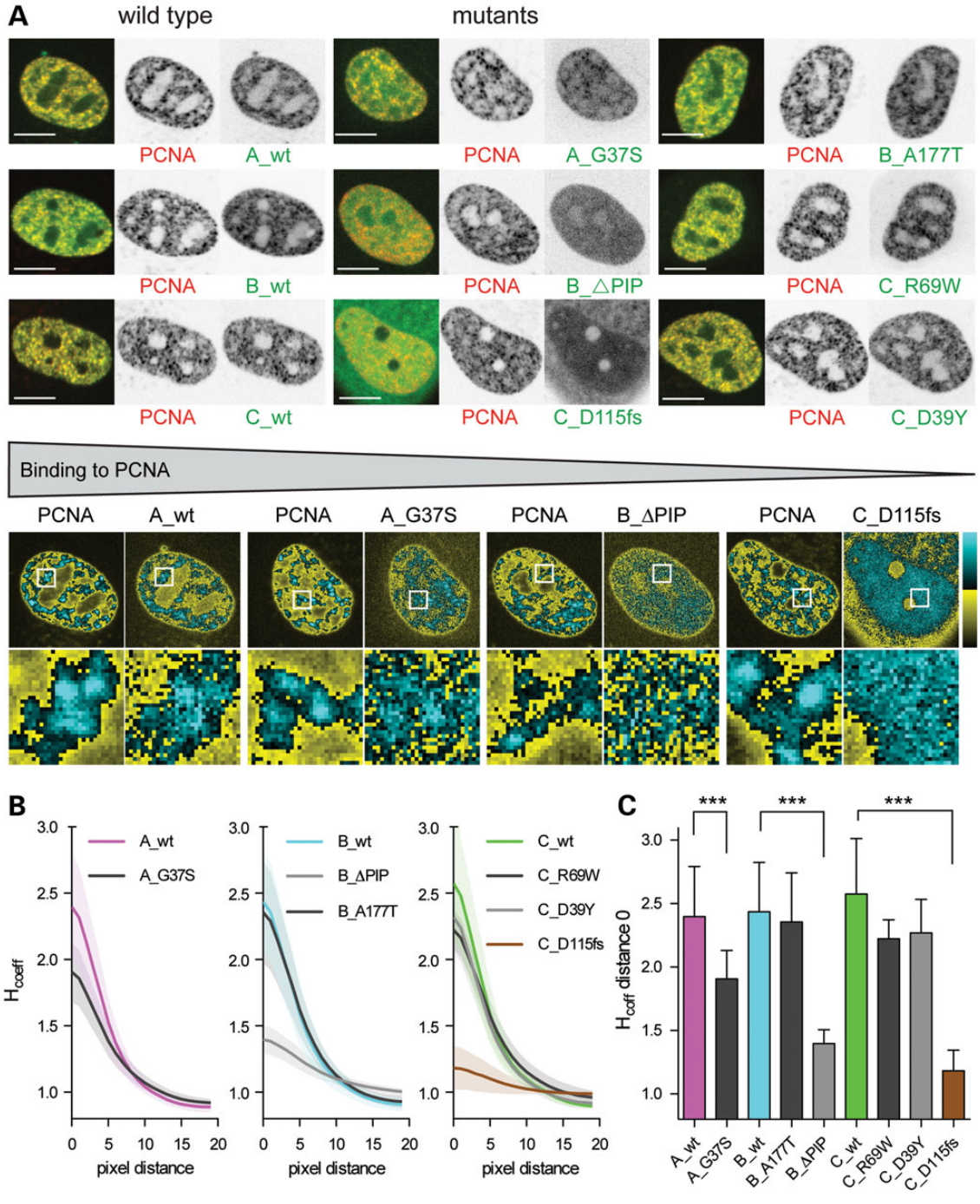


**Figure 4.** Recruitment of RNase H2 to sites of DNA replication. (**A**) Live-cell imaging of S phase HeLa cells expressing mCherry-PCNA and GFP-RNase H2 subunits along with the corresponding untagged subunits. For better visualization, gray images are also shown false color-encoded. Pixel intensity values 0–127 yellow, 128–255 turquoise. Scale bar: 10 μm. (**B**) Quantification of colocalization of RNase H2 subunits and PCNA using $H_{coeff}$ in response to pixel distance. (**C**) $H_{coeff}$ at distance 0 pixel. Wilcoxon–Mann–Whitney test, $^{*}P < 0.05$, $^{**}P < 0.01$, $^{***}P < 0.001$. Indicated are the means ± standard deviation of at least five cells measured in at least two independent experiments.

binding of RNase H2 at sites of DNA repair and replication. This is supported by structural data showing that the A_G37S mutation distorts binding to the active site (17). Accordingly, the A_G37S can still bind to a relatively wider minor groove present in an RNA:DNA hybrid with a longer stretch of ribonucleotides, but not to a more narrower minor groove expected in a DNA:DNA duplex with only a single ribonucleotide (17). This is in line with previous findings showing that recognition of single ribonucleotides and not PCNA-binding is essential for RER (12). Moreover, the residual accumulation of the B_ΔPIP mutant at replication sites suggests that substrate binding of the catalytic domain of the A subunit slowed down dissociation of B_ΔPIP-containing RNase H2. This is consistent with the notion that initiation of substrate cleavage by RNase H2 during RER is

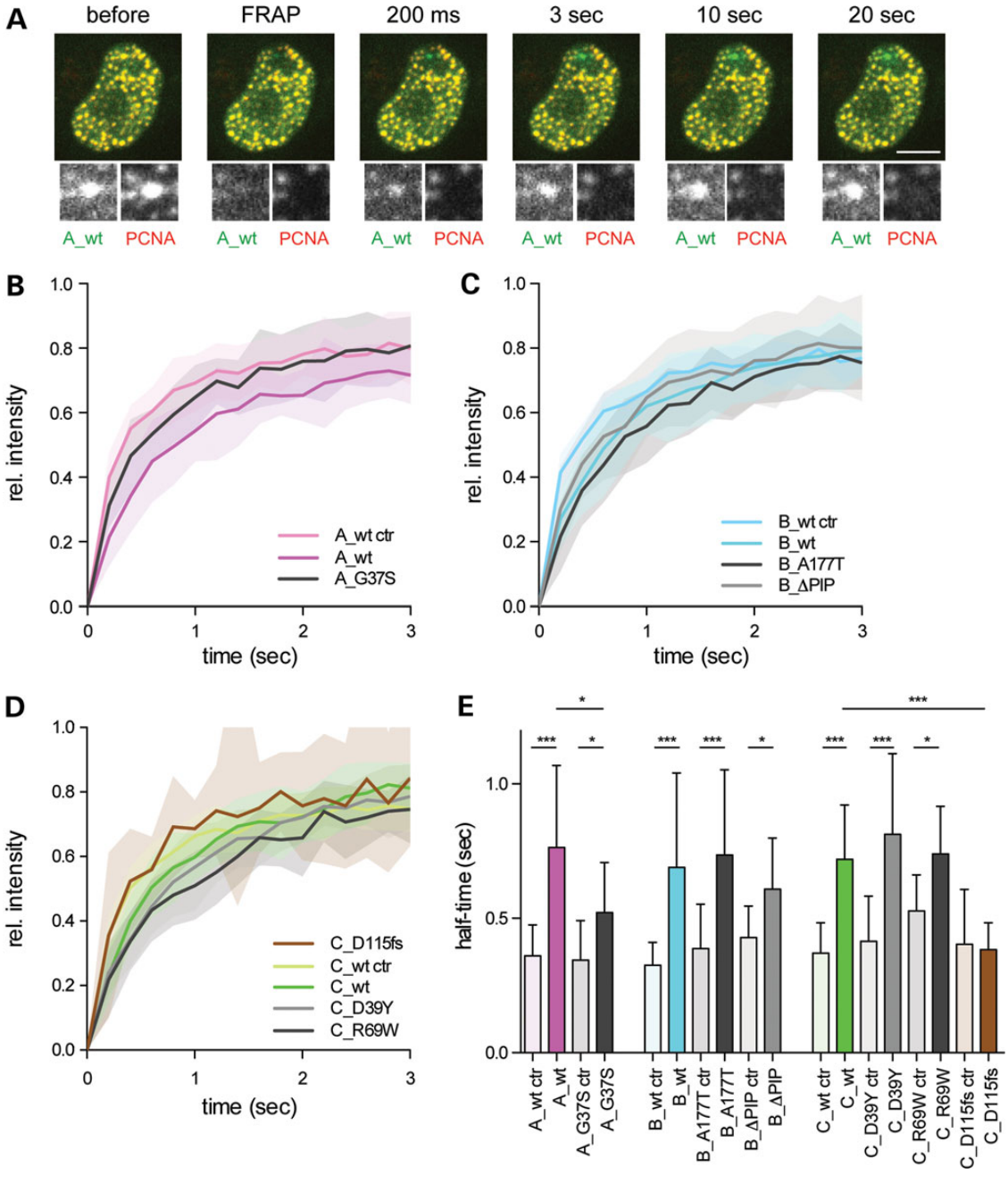


**Figure 5.** Dynamics of RNase H2 at replication sites. (**A**) Live-cell image of a photo-bleached S phase cell expressing mCherry-PCNA (PCNA) and EGFP-RNase H2A (A_wt) along with the untagged B and C subunits. Scale bar: 10 μm. (**B**–**D**) FRAP kinetics of the wild-type and mutated RNase H2 complexes to sites of DNA replication. Control FRAP measurements represent mobility of RNase H2 subunits (A_wt ctr, B_wt ctr, C_wt ctr) in non-S phase cells. Color-shaded areas represent standard deviation. (**E**) Half times determined from FRAP recovery curves. Wilcoxon–Mann–Whitney test, $^{*}P < 0.05$, $^{**}P < 0.01$, $^{***}P < 0.001$. Indicated are the means ± standard deviation of at least five cells measured in at least two independent experiments.

PCNA-independent (6). Catalysis would therefore be more important for retention at replication sites than PCNA binding. Taken together, these findings indicate a catalysis-dependent mechanism by which enzymatically engaged RNase H2 is bound more tightly to replication sites, while the PIP-box is required for consolidating recruitment of RNase H2 to replication forks by its interaction with PCNA. This would imply a two-step mechanism where the PIP-box motif driven interaction with PCNA results in a loose association that generated a localized higher concentration of RNase H2, which in turn can then bind more tightly to the substrate for catalysis. A similar dual mode of recruitment to DNA has been described for DNA methyltransferase (Dnmt1) which also interacts with PCNA via a PIP-box motif. Thus, retention of Dnmt with mutated PIP-box at replication sites was shown to be mediated by an interaction of the targeting sequence domain of Dnmt1 with DNA (41). Likewise, recruitment of poly(ADP-ribose) glycohydrolase (PARG) to DNA involves

both a PCNA-dependent and a poly(ADP-ribose)-dependent mechanism (42).

In mice, complete loss of RNase H2 is embryonic lethal due to DNA damage caused by accumulation of ribonucleotides (3,4). Interestingly, the loss-of-function mutation C_D115fs, predicted to be incompatible with life in the homozygous state, has been described in a compound heterozygous AGS patient along with the C_D39Y mutation (23) which showed no measurable functional alterations in our experimental settings. Although all other AGS-associated mutations studied here, including the common B_A177T and C_R69W, exhibited altered functional properties they were still recruited to sites of DNA damage or repair suggesting that they may have a residual activity and are hypomorphic. Taken together, our findings confirm an essential role of RNase H2 in DNA replication/repair and further suggest that defects in DNA replication/repair due to impaired RNase H2 function contribute to AGS pathogenesis (Fig. 6).

## MATERIALS AND METHODS

### Constructs, cells and transfection

Wild-type RNase H2 subunits cds (RNASEH2A NM_006397, RNASEH2B NM_024570, RNASEH2C NM_032193) were cloned into pEGFP-C1 (Clontech) using *Xho*I and *Hin*dIII. *RNASEH2A*, *RNASEH2B* and *RNASEH2C* mutations identified in AGS patients (A_G37S, B_A177T, C_D39Y, C_R69W, C_D115fs) and the artificial mutation B_ΔPIP (21) were introduced by site-directed mutagenesis (QuikChange Lightning, Agilent Technologies). EGFP was replaced by mCherry or ECFP using *Age*I and *Bsr*GI. HeLa cells were grown at 37°C and 5% $CO_2$ in DMEM supplemented with 10% FCS, 1 μM/ml gentamycin. The medium of HeLa cells stably expressing mCherry-PCNA was supplemented with blasticidin (2.5 μg/ml). Cells were grown on cover slips and co-transfected with 100 ng of fluorescently tagged and 100 ng of corresponding un-tagged RNase H2-constructs using polyethyleneimine as previously described (43).

### Fluorescent cross-correlation spectroscopy

HeLa cells grown on 8-well Lab Tek chamber slides (Nunc) were co-transfected with 10 ng of each EGFP-, mCherry- and ECFP-tagged wild-type or mutant RNase H2 subunits using FuGENE HD (Roche Diagnostics). FCCS was carried out as described in Supplementary Material, Methods using a Zeiss LSM780-Confocor3 microscope of the light microscopy facility BIOTEC/CRTD. For the experiment described in Figure 1B, the following combinations of fluorescent tags were used: for (WT), mCherry-RNase H2A, ECFP-RNase H2B, EGFP-RNase H2C; for (WTΔA), mCherry-RNase H2B, EGFP-RNase H2C; for (WTΔB), mCherry-RNase H2A, EGFP-RNase H2C; for (WTΔC), mCherry-RNase H2A, EGFP-RNase H2B; for (C_D115fs), mCherry-RNase H2A, ECFP-RNase H2B, EGFP-RNase H2C_D115fs.

### Live-cell microscopy, microirradiation and photobleaching experiments

Live-cell imaging, microirradiation and photobleaching experiments were performed using an UltraVIEW VoX spinning disc confocal system (PerkinElmer) in a closed live-cell microscopy chamber (ACU, Perkin Elmer) at 37°C with 5% $CO_2$ and 60% humidity, mounted on a Nikon TI microscope (Nikon). Images were taken with a CFI Apochromat 60x/1.49 NA oil immersion objective. EGFP and mCherry were imaged with 488 and 561 nm laser excitation and 527 ± 55 and 612 ± 70 nm (full width at half maximum) emission filters, respectively. For microirradiation, a preselected spot within the nucleus was microirradiated for 1.2 s with a 405 nm laser set to 100% corresponding to 1 mJ. Before and after microirradiation, confocal

A

| RNase H2 subunit | complex stability | repair binding | repair mobility | replication binding | replication mobility |
|---|---|---|---|---|---|
| A_wt | | ↑ | high | ↑ | low |
| A_G37S | ↓ | ↓ | high | ↓ | intermediate |
| B_wt | | ↑ | high | ↑ | low |
| B_A177T | ↓ | ↑ | high | ↑ | low |
| B_ΔPIP | ↓ | ↓↓↓ | high | ↓↓ | low |
| C_wt | | ↑ | high | ↑ | low |
| C_R69W | ↓ | ↑ | high | ↑ | low |
| C_D39Y | ↑ | ↑ | high | ↑ | low |
| C_D115fs | ↓↓↓ | ↓↓↓ | high | ↓↓↓ | high |

B

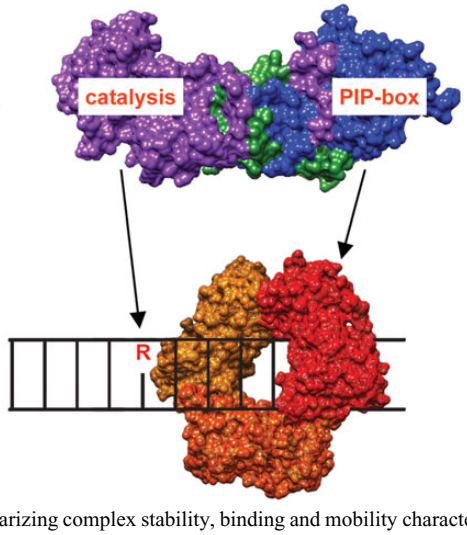


**Figure 6.** Functional properties of RNase H2 during DNA repair and replication. (**A**) Table summarizing complex stability, binding and mobility characteristics of wild-type and mutant RNase H2 subunits. Arrows indicate direction of altered behavior compared with wild-type. High: indicates mobility as fast as unbound protein; low/intermediate: indicates a strong/intermediate delay in turnover. (**B**) Model depicting recruitment of RNase H2 to DNA. The catalytic site is important for direct ribonucleotide substrate binding (R), whereas the PIP-box motif mediates binding to PCNA.

image series of one mid-nuclear section were recorded at 4 s intervals. For evaluation of the accumulation kinetics, the mean intensity of the irradiated region was divided by the mean intensity of the whole nucleus (both corrected for background) using ImageJ. Single exponential functions were used to calculate the plateau. For FRAP analysis, spots of previously microirradiated sites were photo-bleached using a circular ROI (~1.5 μm diameter) at 600 ms with 488 and 561 nm laser set to 100%. Identical bleach regions were selected at sites of DNA replication or repair and in the nucleoplasm (control). Before and after bleaching, confocal image series were recorded at 200 ms time intervals (5 s pre- and 30 s post-bleach). Double normalization was performed in ImageJ as previously described (44,45) and half-times were calculated from these curves using single exponential functions. For colocalization analysis, one confocal plane of living cells was imaged using constant settings (488: 30% laser power, 500 ms exposure time; 561: 30% laser power, 400 ms exposure time). Spatially resolved colocalization was calculated using the $H_{coeff}$ as previously described (39) and is described in Supplementary Material, Methods.

### Statistical analysis

Data were analyzed with Wilcoxon–Mann–Whitney test using GraphPad Prism, *P*-values of $<0.05$ were considered significant.

## SUPPLEMENTARY MATERIAL

Supplementary Material is available at *HMG* online.

## ACKNOWLEDGEMENTS

We wish to thank Susan Hunger, Kerstin Engel and Anne Lehmkuhl for excellent technical assistance. We thank Petra Schwille for advice on FCCS and Corella Casas Delucchi for advice on image analysis. We thank Roger Y. Tsien (University of California, San Diego, USA) for pRSET-mCherry plasmid.

*Conflict of Interest statement*. None declared.

## FUNDING

This work was supported by the Deutsche Forschungsgemeinschaft (KFO 249; LE 1074/4-1 to M.L.-K., GRK 1657/1B and 1C to M.C.C. and A.R.) and the Bundesministerium für Bildung und Forschung (02NUK017) to M.C.C.

## REFERENCES

1. Cerritelli, S.M. and Crouch, R.J. (2009) Ribonuclease H: the enzymes in eukaryotes. *FEBS J.*, **276**, 1494–1505.
2. Nick McElhinny, S.A., Kumar, D., Clark, A.B., Watt, D.L., Watts, B.E., Lundstrom, E.B., Johansson, E., Chabes, A. and Kunkel, T.A. (2010) Genome instability due to ribonucleotide incorporation into DNA. *Nat. Chem. Biol.*, **6**, 774–781.
3. Reijns, M.A., Rabe, B., Rigby, R.E., Mill, P., Astell, K.R., Lettice, L.A., Boyle, S., Leitch, A., Keighren, M., Kilanowski, F. *et al.* (2012) Enzymatic removal of ribonucleotides from DNA is essential for mammalian genome integrity and development. *Cell*, **149**, 1008–1022.
4. Hiller, B., Achleitner, M., Glage, S., Naumann, R., Behrendt, R. and Roers, A. (2012) Mammalian RNase H2 removes ribonucleotides from DNA to maintain genome integrity. *J. Exp. Med.*, **209**, 1419–1426.
5. Nick McElhinny, S.A., Watts, B.E., Kumar, D., Watt, D.L., Lundstrom, E.B., Burgers, P.M., Johansson, E., Chabes, A. and Kunkel, T.A. (2010) Abundant ribonucleotide incorporation into DNA by yeast replicative polymerases. *Proc. Natl Acad. Sci. USA*, **107**, 4949–4954.
6. Sparks, J.L., Chon, H., Cerritelli, S.M., Kunkel, T.A., Johansson, E., Crouch, R.J. and Burgers, P.M. (2012) RNase H2-initiated ribonucleotide excision repair. *Mol. Cell*, **47**, 980–986.
7. Clausen, A.R., Zhang, S., Burgers, P.M., Lee, M.Y. and Kunkel, T.A. (2013) Ribonucleotide incorporation, proofreading and bypass by human DNA polymerase delta. *DNA Repair (Amst.)*, **12**, 121–127.
8. Kim, N., Huang, S.N., Williams, J.S., Li, Y.C., Clark, A.B., Cho, J.E., Kunkel, T.A., Pommier, Y. and Jinks-Robertson, S. (2011) Mutagenic processing of ribonucleotides in DNA by yeast topoisomerase I. *Science*, **332**, 1561–1564.
9. Cerritelli, S.M., Chon, H. and Crouch, R.J. (2011) Molecular biology. A new twist for topoisomerase. *Science*, **332**, 1510–1511.
10. Clausen, A.R., Murray, M.S., Passer, A.R., Pedersen, L.C. and Kunkel, T.A. (2013) Structure-function analysis of ribonucleotide bypass by B family DNA replicases. *Proc. Natl Acad. Sci. USA*, **110**, 16802–16807.
11. Tumbale, P., Williams, J.S., Schellenberg, M.J., Kunkel, T.A. and Williams, R.S. (2014) Aprataxin resolves adenylated RNA-DNA junctions to maintain genome integrity. *Nature*, **506**, 111–115.
12. Chon, H., Sparks, J.L., Rychlik, M., Nowotny, M., Burgers, P.M., Crouch, R.J. and Cerritelli, S.M. (2013) RNase H2 roles in genome integrity revealed by unlinking its activities. *Nucleic Acids Res.*, **41**, 3130–3143.
13. Lazzaro, F., Novarina, D., Amara, F., Watt, D.L., Stone, J.E., Costanzo, V., Burgers, P.M., Kunkel, T.A., Plevani, P. and Muzi-Falconi, M. (2012) RNase H and postreplication repair protect cells from ribonucleotides incorporated in DNA. *Mol. Cell*, **45**, 99–110.
14. Arana, M.E., Kerns, R.T., Wharey, L., Gerrish, K.E., Bushel, P.R. and Kunkel, T.A. (2012) Transcriptional responses to loss of RNase H2 in Saccharomyces cerevisiae. *DNA Repair (Amst.)*, **11**, 933–941.
15. Figiel, M., Chon, H., Cerritelli, S.M., Cybulska, M., Crouch, R.J. and Nowotny, M. (2011) The structural and biochemical characterization of human RNase H2 complex reveals the molecular basis for substrate recognition and Aicardi-Goutieres syndrome defects. *J. Biol. Chem.*, **286**, 10540–10550.
16. Rychlik, M.P., Chon, H., Cerritelli, S.M., Klimek, P., Crouch, R.J. and Nowotny, M. (2010) Crystal structures of RNase H2 in complex with nucleic acid reveal the mechanism of RNA-DNA junction recognition and cleavage. *Mol. Cell*, **40**, 658–670.
17. Shaban, N.M., Harvey, S., Perrino, F.W. and Hollis, T. (2010) The structure of the mammalian RNase H2 complex provides insight into RNA.NA hybrid processing to prevent immune dysfunction. *J. Biol. Chem.*, **285**, 3617–3624.
18. Reijns, M.A., Bubeck, D., Gibson, L.C., Graham, S.C., Baillie, G.S., Jones, E.Y. and Jackson, A.P. (2011) The structure of the human RNase H2 complex defines key interaction interfaces relevant to enzyme function and human disease. *J. Biol. Chem.*, **286**, 10530–10539.
19. Jeong, H.S., Backlund, P.S., Chen, H.C., Karavanov, A.A. and Crouch, R.J. (2004) RNase H2 of Saccharomyces cerevisiae is a complex of three proteins. *Nucleic Acids Res.*, **32**, 407–414.
20. Chon, H., Vassilev, A., DePamphilis, M.L., Zhao, Y., Zhang, J., Burgers, P.M., Crouch, R.J. and Cerritelli, S.M. (2009) Contributions of the two accessory subunits, RNASEH2B and RNASEH2C, to the activity and properties of the human RNase H2 complex. *Nucleic Acids Res.*, **37**, 96–110.
21. Bubeck, D., Reijns, M.A., Graham, S.C., Astell, K.R., Jones, E.Y. and Jackson, A.P. (2011) PCNA directs type 2 RNase H activity on DNA replication and repair substrates. *Nucleic Acids Res.*, **39**, 3652–3666.
22. Aicardi, J. and Goutieres, F. (1984) A progressive familial encephalopathy in infancy with calcifications of the basal ganglia and chronic cerebrospinal fluid lymphocytosis. *Ann. Neurol.*, **15**, 49–54.
23. Ramantani, G., Kohlhase, J., Hertzberg, C., Innes, A.M., Engel, K., Hunger, S., Borozdin, W., Mah, J.K., Ungerath, K., Walkenhorst, H. *et al.* (2010) Expanding the phenotypic spectrum of lupus erythematosus in Aicardi-Goutieres syndrome. *Arthritis Rheum.*, **62**, 1469–1477.
24. Crow, Y.J., Hayward, B.E., Parmar, R., Robins, P., Leitch, A., Ali, M., Black, D.N., van, B.H., Brunner, H.G., Hamel, B.C. *et al.* (2006) Mutations in the gene encoding the 3′-5′ DNA exonuclease TREX1 cause Aicardi-Goutieres syndrome at the AGS1 locus. *Nat. Genet.*, **38**, 917–920.

25. Rice, G.I., Bond, J., Asipu, A., Brunette, R.L., Manfield, I.W., Carr, I.M., Fuller, J.C., Jackson, R.M., Lamb, T., Briggs, T.A. *et al.* (2009) Mutations involved in Aicardi-Goutieres syndrome implicate SAMHD1 as regulator of the innate immune response. *Nat. Genet.*, **41**, 829–832.
26. Rice, G.I., Kasher, P.R., Forte, G.M., Mannion, N.M., Greenwood, S.M., Szynkiewicz, M., Dickerson, J.E., Bhaskar, S.S., Zampini, M., Briggs, T.A. *et al.* (2012) Mutations in ADAR1 cause Aicardi-Goutieres syndrome associated with a type I interferon signature. *Nat. Genet.*, **44**, 1243–1248.
27. Rice, G.I., Del Toro, D.Y., Jenkinson, E.M., Forte, G.M., Anderson, B.H., Ariaudo, G., Bader-Meunier, B., Baildam, E.M., Battini, R., Beresford, M.W. *et al.* (2014) Gain-of-function mutations in IFIH1 cause a spectrum of human disease phenotypes associated with upregulated type I interferon signaling. *Nat. Genet.*, **46**, 503–509.
28. Rice, G., Patrick, T., Parmar, R., Taylor, C.F., Aeby, A., Aicardi, J., Artuch, R., Montalto, S.A., Bacino, C.A., Barroso, B. *et al.* (2007) Clinical and molecular phenotype of Aicardi-Goutieres syndrome. *Am. J. Hum. Genet.*, **81**, 713–725.
29. Lee-Kirsch, M.A., Chowdhury, D., Harvey, S., Gong, M., Senenko, L., Engel, K., Pfeiffer, C., Hollis, T., Gahr, M., Perrino, F.W. *et al.* (2007) A mutation in TREX1 that impairs susceptibility to granzyme A-mediated cell death underlies familial chilblain lupus. *J. Mol. Med. (Berl.)*, **85**, 531–537.
30. Ravenscroft, J.C., Suri, M., Rice, G.I., Szynkiewicz, M. and Crow, Y.J. (2011) Autosomal dominant inheritance of a heterozygous mutation in SAMHD1 causing familial chilblain lupus. *Am. J. Med. Genet. A.*, **155A**, 235–237.
31. Lee-Kirsch, M.A., Gong, M., Chowdhury, D., Senenko, L., Engel, K., Lee, Y.A., de, S.U., Bailey, S.L., Witte, T., Vyse, T.J. *et al.* (2007) Mutations in the gene encoding the 3′-5′ DNA exonuclease TREX1 are associated with systemic lupus erythematosus. *Nat. Genet.*, **39**, 1065–1067.
32. Behrendt, R. and Roers, A. (2014) Mouse models for Aicardi-Goutieres syndrome provide clues to the molecular pathogenesis of systemic autoimmunity. *Clin. Exp. Immunol.*, **175**, 9–16.
33. Lee-Kirsch, M.A., Wolf, C. and Gunther, C. (2014) Aicardi-Goutieres syndrome: a model disease for systemic autoimmunity. *Clin. Exp. Immunol.*, **175**, 17–24.
34. Coffin, S.R., Hollis, T. and Perrino, F.W. (2011) Functional consequences of the RNase H2A subunit mutations that cause Aicardi-Goutieres syndrome. *J. Biol. Chem.*, **286**, 16984–16991.
35. Perrino, F.W., Harvey, S., Shaban, N.M. and Hollis, T. (2009) RNaseH2 mutants that cause Aicardi-Goutieres syndrome are active nucleases. *J. Mol. Med. (Berl.)*, **87**, 25–30.
36. Maga, G. and Hubscher, U. (2003) Proliferating cell nuclear antigen (PCNA): a dancer with many partners. *J. Cell Sci.*, **116**, 3051–3060.
37. Mortusewicz, O. and Leonhardt, H. (2007) XRCC1 and PCNA are loading platforms with distinct kinetic properties and different capacities to respond to multiple DNA lesions. *BMC Mol. Biol.*, **8**, 81.
38. Mortusewicz, O., Rothbauer, U., Cardoso, M.C. and Leonhardt, H. (2006) Differential recruitment of DNA Ligase I and III to DNA repair sites. *Nucleic Acids Res.*, **34**, 3523–3532.
39. Herce, H.D., Casas-Delucchi, C.S. and Cardoso, M.C. (2013) New image colocalization coefficient for fluorescence microscopy to quantify (bio-)molecular interactions. *J. Microsc.*, **249**, 184–194.
40. Sporbert, A., Gahl, A., Ankerhold, R., Leonhardt, H. and Cardoso, M.C. (2002) DNA polymerase clamp shows little turnover at established replication sites but sequential de novo assembly at adjacent origin clusters. *Mol. Cell*, **10**, 1355–1365.
41. Schneider, K., Fuchs, C., Dobay, A., Rottach, A., Qin, W., Wolf, P., varez-Castro, J.M., Nalaskowski, M.M., Kremmer, E., Schmid, V. *et al.* (2013) Dissection of cell cycle-dependent dynamics of Dnmt1 by FRAP and diffusion-coupled modeling. *Nucleic Acids Res.*, **41**, 4860–4876.
42. Mortusewicz, O., Fouquerel, E., Ame, J.C., Leonhardt, H. and Schreiber, V. (2011) PARG is recruited to DNA damage sites through poly(ADP-ribose)- and PCNA-dependent mechanisms. *Nucleic Acids Res.*, **39**, 5045–5056.
43. Casas-Delucchi, C.S., Becker, A., Bolius, J.J. and Cardoso, M.C. (2012) Targeted manipulation of heterochromatin rescues MeCP2 Rett mutants and re-establishes higher order chromatin organization. *Nucleic Acids Res.*, **40**, e176.
44. Phair, R.D., Gorski, S.A. and Misteli, T. (2004) Measurement of dynamic protein binding to chromatin in vivo, using photobleaching microscopy. *Methods Enzymol.*, **375**, 393–414.
45. Sprague, B.L. and McNally, J.G. (2005) FRAP analysis of binding: proper and fitting. *Trends Cell Biol.*, **15**, 84–91.

**Altered spatio-temporal dynamics of RNase H2 complex assembly at replication and repair sites in Aicardi-Goutières syndrome**

Barbara Kind [1,†], Britta Muster [2,†], Wolfgang Staroske [3], Henry D. Herce [4], René Sachse [5], Alexander Rapp [2], Franziska Schmidt [1], Sarah Koss [1], M. Cristina Cardoso [2*], Min Ae Lee-Kirsch [1 *]

[1] Department of Pediatrics, Medizinische Fakultät Carl Gustav Carus, Technische Universität Dresden, 01307 Dresden, Germany

[2] Department of Biology, Technische Universität Darmstadt, 64287 Darmstadt, Germany

[3] Biotechnology Center, Technische Universität Dresden, 01307 Dresden, Germany

[4] Department of Physics, Applied Physics and Astronomy, Rensselaer Polytechnic Institute; New York 12180-3590, USA

[5] Institute of Earth and Environmental Science, Potsdam University, 14476 Potsdam, Germany

Corresponding authors:

Min Ae Lee-Kirsch, Department of Pediatrics, Medizinische Fakultät Carl Gustav Carus, Technische Universität Dresden, 01307 Dresden, Germany, phone: +49-351-458 6878, fax: +49-351-458 6333; email: minae.lee-kirsch@uniklinikum-dresden.de

M. Cristina Cardoso, Department of Biology, Technische Universität Darmstadt, 64287 Darmstadt, Germany, phone: +49-6151-16-2377; fax: +49-6151-16-2375; email: cardoso@bio.tu-darmstadt.de

[†] Equally contributing authors

## SUPPLEMENTARY METHODS

### FCCS data acquisition

Fluorescence cross-correlation spectroscopy (FCCS) and laser scanning microscopy were carried out on a commercial confocal microscope Zeiss LSM780 with an attached Confocor 3 at the light microscopy facility BIOTEC/CRTD. The 488 nm Ar-laser-line was used to excite EGFP and the 561 nm line was used to excite mCherry. Both laser lines were attenuated by an acousto-optical tunable filter to intensities in the focal plane of 1.6 kW/cm² (GFP) and 2.6 kW/cm² (mCherry), respectively. Both excitation laser lines were directed by a 488 / 561 dichroic mirror (MBS) onto the back aperture of a Zeiss C-Apochromat 40x, N.A. = 1.2, water immersion objective. The fluorescence light was collected by the same objective, separated from the excitation light by the MBS, passing a confocal pinhole (35 µm in diameter) and split into two spectral channels by a second dichroic (NFT, LP565). After removing residual laser light by a 495-555 nm bandpass and 580 nm longpass emission filter, respectively, the fluorescence light was recorded by avalanche photodiode detectors (APDs). Before each experiment the setup was adjusted using a dye mixture of Alexa488 and CF568 and a 198 bp long Alexa488 / Atto565 double labelled DNA, yielding cross-correlation amplitudes of 80 % (± 5 %). The discrepancy to 100 % is due to imperfect overlap of the detection volumes and/ or imperfect labelling of the DNA (1;2;3;4). Therefore, even in presence of a perfect interaction, cross-correlation values would not reach 100 %.

For intracellular FCCS, a confocal image was acquired and the FCCS focus was positioned inside the nucleus approximately 3 µm above the cover slip. For each measurement, 24 runs, each 10 seconds long were collected. Cells were kept in air-buffer (150 mM NaCl, 20 mM HEPES pH 7.4, 15 mM glucose, 150 µg/ml BSA, 20 mM trehalose, 5.4 mM KCl, 0.85 mM MgSO4, 0.6 mM $CaCl_2$) at room temperature during measurement (5). Confocal imaging was performed using the 32 channel GaAsP detector of the Zeiss LSM780 in photon counting mode.

### FCCS data analysis

The fluorescence signals of each run were software correlated by the Zeiss ZEN Software following the definition of auto- and cross-correlation (1;2;3)

$$G_{ij}(\tau) = \frac{\left\langle \delta F_i(t) \cdot \delta F_j(t+\tau) \right\rangle}{\left\langle F_i(t) \right\rangle \left\langle F_j(t) \right\rangle}$$

.

Runs showing diffusion of remaining cellular compartments were discarded from the data evaluation.

A model including two diffusing species and a term accounting for the photophysics was fitted to the two auto-correlation and the cross-correlation curves, using a weighted Marquardt non-linear least square fitting algorithm. The cross-correlation curve was the average of the two cross-correlation curves (red vs. green and green vs. red channel).

$$G_{ij}(\tau) = G_{ij}(0) \cdot \left(1 + \frac{T}{1-T}\right) \cdot e^{\left(-\tau/\tau_T\right)} \cdot \left( \frac{F}{\left(1+\frac{\tau}{\tau_1}\right)\sqrt{1+\frac{\tau}{S^2 \cdot \tau_1}}} + \frac{1-F}{\left(1+\frac{\tau}{\tau_2}\right)\sqrt{1+\frac{\tau}{S^2 \cdot \tau_2}}} \right)$$

T represents the fraction of molecules in the dark state, $\tau_T$ the lifetime of the dark state, $\tau_1$ and $\tau_2$ are the diffusion times of the two species, F is the fraction of the two species and S is the form factor, which is the ratio of axial ($\tau_z$) over the radial radius ($\tau_{xy}$). During the fit the triplet fraction T of the cross-correlation curve was fixed to zero.

The amplitudes $G_{ij}(0)$ were corrected for spurious autofluorescent background of the cells, using the following algorithm:

$$\tilde{G}_{ij}(0) = G_{ij}(0) \frac{F_i}{F_i - B_i} \cdot \frac{F_j}{F_j - B_j}$$

Here, F is the measured count rate and B the measured background count rate, which was measured in HeLa cells transfected with an empty vector. The background in the green channel was below 1% of the measured fluorescent signal and for the red channel between 1 and 2%. In addition, background corrected amplitudes, $\tilde{G}_{ij}(0)$, were corrected for spectral crosstalk. Spectral crosstalk was only encountered from the green into the red channel, with an amount of $\beta = 9.8\ \%$. Subsequently, the green amplitude is unaffected, while the red and the cross-correlation amplitude need to be corrected for spectral crosstalk:

$$\hat{G}_g(0) = G_g(0)$$

$$\hat{G}_r(0) = \frac{F_r^2 G_r(0) + \beta^2 F_g^2 G_g(0) - 2\beta F_r F_g G_{CC}(0)}{\left(F_r - \beta F_g\right)^2}$$

$$\hat{G}_{CC}(0) = \frac{F_r F_g G_{CC}(0) - \beta F_g^2 G_g(0)}{\left(F_g F_r - \beta F_g\right)^2}$$

From the corrected amplitudes, the number of fluorescent particles in the detection volume was calculated, which is given by the following set of formulas:

$$\hat{G}_g(0) = \frac{1}{N_g + N_{gr}}; \hat{G}_r(0) = \frac{1}{N_r + N_{gr}}; \hat{G}_{CC}(0) = \frac{N_{gr}}{(N_g + N_{gr})(N_r + N_{gr})}$$

Here, $N_g$ is the number of only green labelled particles, $N_r$ the number of only red labelled particles and $N_{gr}$ the number of particles, which carry both labels. For analysis of FCCS data only measurements with molecule numbers N < 150 within the confocal volume were included.

The amount of cross-correlation was calculated by dividing the number of double labelled particles by all particles carrying a green label:

$$CC = \frac{N_{gr}}{N_g + N_{gr}}$$

**$H_{coeff}$ data analysis**

The $H_{coeff}$ shows the spatial correlation between two fluorescent molecules as a function of the distance between the molecules described by the following relation:

$$H_{coeff}(r) = \frac{N_p \sum_{i=1}^{N_p} (Ir_i \sum_{r<\Delta ij<r+\Delta} Ig_j)}{(\sum_{i=1}^{N_p} Ir_i)((\sum_{i=1}^{Np} Ig_i)(\sum_{r<\Delta ij<r+\Delta} 1)}$$

Where $Ir_i$ and $Ig_i$ is the intensity of the channels *r* and *g* in the pixel *i* and $N_p$ is the total number of pixels (accessible to the molecules, in our case the nucleus), Δ is the thickness of the interval evaluated at a distance *r* and $\Delta_{ij}$ is the distance between the pixel *i* and pixel *j*. The divisor is used to normalize the equation by the number of pixels counted in the g channel for each distance *r*. $H_{coeff}$ at pixel 0 means direct colocalization at the given pixel, whereas increasing pixel distance reflects colocalization with the surrounding pixels. This coefficient (or rather its logarithm) was specifically designed to parametrize the strength of molecular interactions extracted from fluorescent signals in a thermodynamics sense (6). If the proteins repel each other, or are anticorrelated, $H_{coeff}$ <1 ($Log(H_{coeff})$ < 0), if they do not interact, or are randomly correlated, $H_{coeff}$ = 1 ($Log(H_{coeff})$=0) and if the proteins attract each other, or are correlated, $H_{coeff}$ >1 ($Log(H_{coeff})$ > 0).

**Supplementary References**


1. Schwille,P., Meyer-Almes,F.J. and Rigler,R. (1997) Dual-color fluorescence cross-correlation spectroscopy for multicomponent diffusional analysis in solution. Biophys. J., 72, 1878-1886.

2. Bacia,K., Kim,S.A. and Schwille,P. (2006) Fluorescence cross-correlation spectroscopy in living cells. Nat. Methods, 3, 83-89.

3. Bacia, K., Petrášek, Z. & Schwille, P. (2012) Correcting for Spectral Cross-Talk in Dual-Color Fluorescence Cross-Correlation Spectroscopy. Chemphyschem, *13*, 1221-1231.

4. Foo,Y.H., Naredi-Rainer,N., Lamb,D.C., Ahmed,S. and Wohland,T. (2012) Factors affecting the quantification of biomolecular interactions by fluorescence cross-correlation spectroscopy. Biophys. J., 102, 1174-1183.

5. Ohrt T., Staroske W., Muetze J., Crell K., Landthaler M., Schwille P. (2011) Fluorescence cross-correlation spectroscopy reveals mechanistic insights into the effect of 2'-O-methyl modified siRNAs in living cells. Biophys. J. 100, 2981-2990.

6. Herce,H.D., Casas-Delucchi,C.S., Cardoso,M.C. (2013) New image colocalization coefficient for fluorescence microscopy to quantify (bio-)molecular interactions. J Microsc., 249, 184-194.

**Supplementary Figure 1**

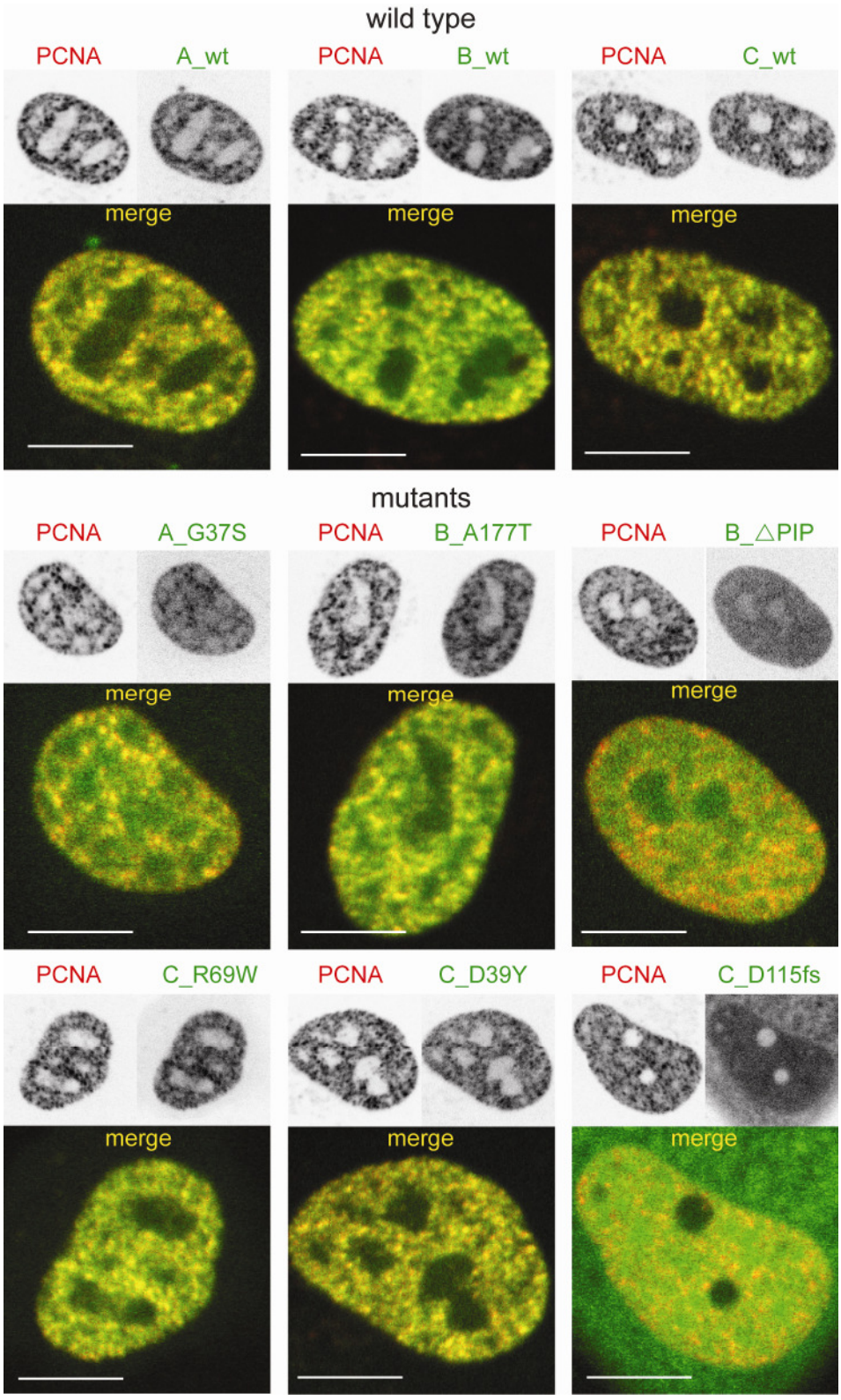


**Supplementary Figure S1.** Recruitment of RNase H2 to sites of DNA replication. Live-cell imaging of S phase HeLa cells expressing mCherry-PCNA and GFP-RNase H2 subunits along with the untagged A and C subunits.